EUROPEAN ORGANIZATION FOR NUCLEAR RESEARCH

L3 Internal Note 2254
May 4, 1998

Search for Neutral Higgs Bosons of the Minimal Supersymmetric Standard Model in e^+e^- Interactions at $\sqrt{s} = 130 - 183$ GeV

J. G. Branson[∮], F. Di Lodovico[♯], A. Dominguez[∮], I. Fisk[∮], G. Raven[∮]
∮ University of California, San Diego
♯ ETH, Zürich

Abstract

A search for the lightest neutral scalar and pseudoscalar Higgs bosons in the Minimal Supersymmetric Standard Model is performed on data collected at LEP by the L3 detector at center-of-mass energies $130 \leq \sqrt{s} \leq 183$ GeV. No significant excess is observed. Limits on the mass of the lightest neutral Higgs boson are given as a function of $\tan\beta$. Lower mass limits are set at the 95% confidence level at $m_{\mathrm{H}} > 70.7$ GeV and $m_{\mathrm{A}} > 71.0$ GeV.

Introduction

Despite its remarkable phenomelogical success, it is necessary to regard the Standard Model (SM) as an effective low–energy theory, valid up to some energy scale Λ at which it is replaced by some more fundamental theory [1], due to the *naturaless* or *hierarchy* problem. Supersymmetry [2, 6] which presupposes a symmetry between fermions and bosons, assuming that each particle with spin j has a supersymmetric patner with spin j–1/2, is introduced because of its improved ultraviolet behaviour with respect to ordinary quantum field theory, due to cancellations between bosonic and fermionic loop diagrams. The most economical realization of the low–energy supersymmetry, i.e. supersymmetry effectively broken at the electroweak scale, is the Minimal Supersymmetric Standard Model (MSSM). The gauge group is $\mathrm{SU}(3)_C \otimes \mathrm{SU}(2)_L \otimes \mathrm{U}(1)_Y$, and the matter content corresponds to three generations of quarks and leptons as in the Standard Model.

To proceed torwards a realistic model, one has to introduce supersymmetry breaking. To give masses to all charged fermions and to avoid chiral anomalies, one is forced to introduce two complex Higgs doublets one more than in the Standard Model case. The physical states are three neutral bosons (two CP–even, h^0 and H^0, and one CP–odd, A^0) and a charged boson ($\mathrm{H}^{\pm}$). At the tree level, all Higgs masses and couplings can be expressed in terms of two parameters only. For example m_{A}, $\tan\beta$, where $\tan\beta$ is the ratio of the vacuum expectation values of the two Higgs doublets. Moreover, there is at least one neutral CP–even Higgs boson (h^0) with mass smaller than the mass of the Z boson, significantly coupled with it. However, Higgs boson masses are subject to positive and large radiative corrections, dominated by loops involving the top quark and its supersymmetric patners. Different methods, implying a variety of different approximations exist to compute radiative corrections to the Higgs boson masses. Among them, there is the renormalization group approach, which is used in this paper [7].
The main production mechanisms of the neutral Higgs bosons h and A in the MSSM at LEP2 energies are the following processes:

(a) Higgs-strahlung: $\mathrm{e}^+\mathrm{e}^- \to \mathrm{hZ}$,

(b) associated pair–production: $\mathrm{e}^+\mathrm{e}^- \to \mathrm{hA}$.

The fusion processes, similar to those in the Standard Model, play only a marginal role at the kinematical limit of the Higgs–strahlung process for the production of the CP–even Higgs boson h. The Higgs boson A cannot be produced in the Higgs–strahlung or in fusion processes to leading order, due to its CP–odd nature. The production of the heavy CP–even Higgs particle H is very difficult at LEP energies.

The cross sections for the two processes (a) and (b) can be expressed in terms of the cross section σ_{SM} for Higgs–strahlung in the Standard Model in the following way:

$$\sigma(\mathrm{e}^+\mathrm{e}^- \to \mathrm{hZ}) = \sin^2(\beta-\alpha)\sigma_{\mathrm{SM}}$$
$$\sigma(\mathrm{e}^+\mathrm{e}^- \to \mathrm{Ah}) = \cos^2(\beta-\alpha)\overline{\lambda}\sigma_{\mathrm{SM}}$$

where α is the mixing angle in the neutral sector. The factor

$$\overline{\lambda} = \lambda_{\mathrm{hA}}^{3/2}/[\lambda_{\mathrm{hZ}}^{1/2}(12m_{\mathrm{Z}}^2/s + \lambda_{\mathrm{hZ}})]$$

accounts for the correct suppression of the P–wave cross section near the thresholds [$\lambda_{\mathrm{ij}} = (1-(m_1+m_{\mathrm{j}})^2/s)(1-(m_2-m_{\mathrm{i}})^2)/s$ is the usual momentum factor of the two–particle phase space].

The cross sections for the Higgs–strahlung and the associated pair–production are complementary to each other, coming either with the coefficient $\sin^2(\beta-\alpha)$ or $\cos^2(\beta-\alpha)$, respectively. For small $\tan\beta$ the Higgs–strahlung provides the largest production cross section, while the cross section for hA associated pair–production is much smaller. For large $\tan\beta$ the hA pair–production is the dominant mechanism. For $\tan\beta > 1$, the lightest CP–even neutral Higgs boson h decays almost exclusively to a fermion–pair if the mass m_h is less than 100 GeV. Near the upper limit of m_h for a given $\tan\beta$, the decay pattern becomes Standard Model–like. Fermion–pairs are also the dominant decay mode of the pseudoscalar A.

In case of neutral pair–production, the dominant decay channels are by far $\mathrm{b\bar{b}b\bar{b}}$ and $\tau^+\tau^-\mathrm{b\bar{b}}$, as soon as the decay modes into a $\tau^+\tau^-$ or $\mathrm{b\bar{b}}$ pair are open. The branching ratio for A (h) $\rightarrow \mathrm{b\bar{b}}$, $\tau^+\tau^-$ is $\sim 92\%$ and $\sim 7\%$ respectively. The hA topologies are very similar to their hZ counterparts ($\mathrm{e^+e^-} \rightarrow \mathrm{hZ} \rightarrow \mathrm{q\bar{q}\,q'\bar{q}'}$, $\tau^+\tau^-\,\mathrm{b\bar{b}}$, $\tau^+\tau^-\,\mathrm{q\bar{q}}$), but the Z-mass constraint cannot be used and, on average, these events are more likely to contain b hadrons. A global analysis for both for Higgs–strahlung and neutral–pair production is then needed.

This paper analyzes the neutral Higgs boson production $\mathrm{e^+e^-} \rightarrow \mathrm{hA}$, where the two Higgs bosons decay either both in a $\mathrm{b\bar{b}}$ pair or one in a $\tau^+\tau^-$ pair and the other in a $\mathrm{b\bar{b}}$ pair, and the Higgs–strahlung production in the $\mathrm{q\bar{q}\,q'\bar{q}'}$, $\tau^+\tau^-\,\mathrm{b\bar{b}}$ and $\tau^+\tau^-\,\mathrm{q\bar{q}}$ final states.

Data and Monte Carlo Samples

The data were collected by the L3 detector [8–16] at LEP from 1995 to 1997. The integrated luminosities are 6.1, 5.9 10.8, 10.2 and 55.3 pb^{-1} at the average center-of-mass energies of 130.3, 136.3, 161.3, 172.3 and 182.7 GeV, respectively.

The signal cross sections and branching ratios were calculated using the HZHA generator [17]. For the efficiency studies, Monte Carlo samples of Higgs events were generated using PYTHIA [18,19]. For the background studies, the following Monte Carlo programs were used: PYTHIA ($\mathrm{e^+e^-} \rightarrow \mathrm{q\bar{q}}$), KORALW [20] ($\mathrm{e^+e^-} \rightarrow \mathrm{W^+W^-}$), KORALZ [21] ($\mathrm{e^+e^-} \rightarrow \tau^+\tau^-$), PYTHIA and PHOJET [22] ($\mathrm{e^+e^-} \rightarrow \mathrm{e^+e^-q\bar{q}}$), and EXCALIBUR [23] ($\mathrm{e^+e^-} \rightarrow \mathrm{f\,\bar{f}'f\,\bar{f}'}$). The number of simulated background events for the most important background channels is typically 100 times the number of collected data events.

The L3 detector response is simulated using the GEANT 3.15 program [24], which takes into account the effects of energy loss, multiple scattering and showering in the detector. The GHEISHA program [25] is used to simulate hadronic interactions in the detector.

Analysis Procedures

A global analysis for both for Higgs–strahlung and neutral–pair production is performed. The other channels of the Higgs–strahlung production ($\mathrm{e^+e^-} \rightarrow \mathrm{hZ} \rightarrow \mathrm{e^+e^-q\bar{q}}$, $\mu^+\mu^-\mathrm{q\bar{q}}$, $\nu\bar{\nu}\mathrm{q\bar{q}}$) are instead the same already studied and published in [26]. The analyses of hA and hZ decays are performed in three stages. First, a high multiplicity hadronic event selection is chosen. This greatly reduces background events with large missing energy and low multiplicity while maintaining a high signal efficiency over a broad range of possible Higgs masses. Second, a set of cuts tailored to the specific Higgs decay in question is chosen using an automated optimization procedure [28,29]. These cuts are optimized for each center-of-mass energy. Third, a discriminating variable is built for each analysis which depends on the mass hypothesis and relative production rates of hA and hZ. The spectrum of this discriminant is recomputed for each point in the $(\tan\beta, m_{\mathrm{A}})$ scan and is used in the likelihood calculation which tests for the presence of a signal. The b-tagging variable plays a large role in the calculation of this discriminant.

In the following, first the B–tagging is descrided, then the analyses deviced to the four–jet channels and to the tau channels are described and the results are shown.

B-tagging

Jets containing b quarks are primarily identified with lifetime information. The confidence level, C_N, that a set of N tracks originated from the primary vertex is constructed using the decay length significance of each track. First the crossing point of each track with the closest jet is determined in both the $r\phi$ and rz projections. Then the signed distances between these crossing points and the reconstructed event primary vertex are projected onto the jet axis to determine the decay length, L. If the probability that both $r\phi$ and rz measurements are compatible exceeds 5%, then the two are combined. Otherwise, the $r\phi$ projection is used.

The confidence level is calculated in two ways. The first approach takes into account the fraction of tracks with positive decay length,

$$C_N = \frac{\Pi}{2^N} \sum_{i=0}^{N-1} \sum_{j=i+1}^{N} \binom{N}{j} \frac{(-\log\Pi)^i}{i!}, \quad \Pi = \prod_{j=1}^{N_+} P_j(L/\sigma_L),$$

where N_+ is the number of tracks with positive decay length. The probability that a track originated from the primary vertex, $P(L/\sigma_L)$, is obtained from the control sample of tracks with negative decay length. The second approach weights each $P(L/\sigma_L)$ by a power α depending on the decay length resolution and momentum of the track,

$$C'_N = 1 - \int_{l_{N_+}}^{1} dx_{N_+} \cdots \int_{l_1}^{1} dx_1, \quad l_j = \left(\frac{\mathcal{P}}{\prod_{i=j+1}^{N_+} x_i^{\alpha_i}} \right)^{\frac{1}{\alpha_j}}, \quad \mathcal{P} = \prod_{j=1}^{N_+} P_j^{\alpha_j}(L/\sigma_L).$$

By construction, the distributions of both variables are flat for events without lifetime, whereas events containing tracks originating from secondary vertices peak at zero.

To improve the tagging efficiency, the two lifetime variables, C_N and C'_N, are combined with other discriminating information using a neural network. The network has fourteen inputs. These include variables computed from reconstructed secondary vertices, such as invariant mass and multiplicity; jet shape variables, e.g. boosted sphericity and $\beta\gamma$; and if an identified electron or muon is present, its momentum information.

The neural network output for a set of jets is combined into an event tag by computing the probability that each jet is compatible with the distribution for light quarks determined from Monte Carlo. The B_{tag} variable is defined as the negative log-likelihood of these probabilities. As an example, the B_{tag} spectrum for the sample of $\mathrm{e^+e^-} \rightarrow \mathrm{Z} \rightarrow \mathrm{q\bar{q}}$ events taken during the 1997 calibration run at 91 GeV is presented in Figure 1 (a). The efficiency and purity for $\mathrm{Z} \rightarrow \mathrm{b\bar{b}}$ events are shown in Figure 1 (b) as functions of the cut on B_{tag}.
More detail about the B–tagging algorithm can be found in [27].

The $\mathbf{hA \rightarrow b\bar{b}\,b\bar{b}}$ and $\mathbf{hZ \rightarrow b\bar{b}\,q\bar{q}}$ channels

The signature of both the $\mathrm{hA} \rightarrow \mathrm{b\bar{b}b\bar{b}}$ and $\mathrm{hZ} \rightarrow \mathrm{b\bar{b}q\bar{q}}$ decay modes is four high multiplicity hadronic jets and the presence of b hadron decay products. In the case of $\mathrm{hA} \rightarrow \mathrm{b\bar{b}b\bar{b}}$ the

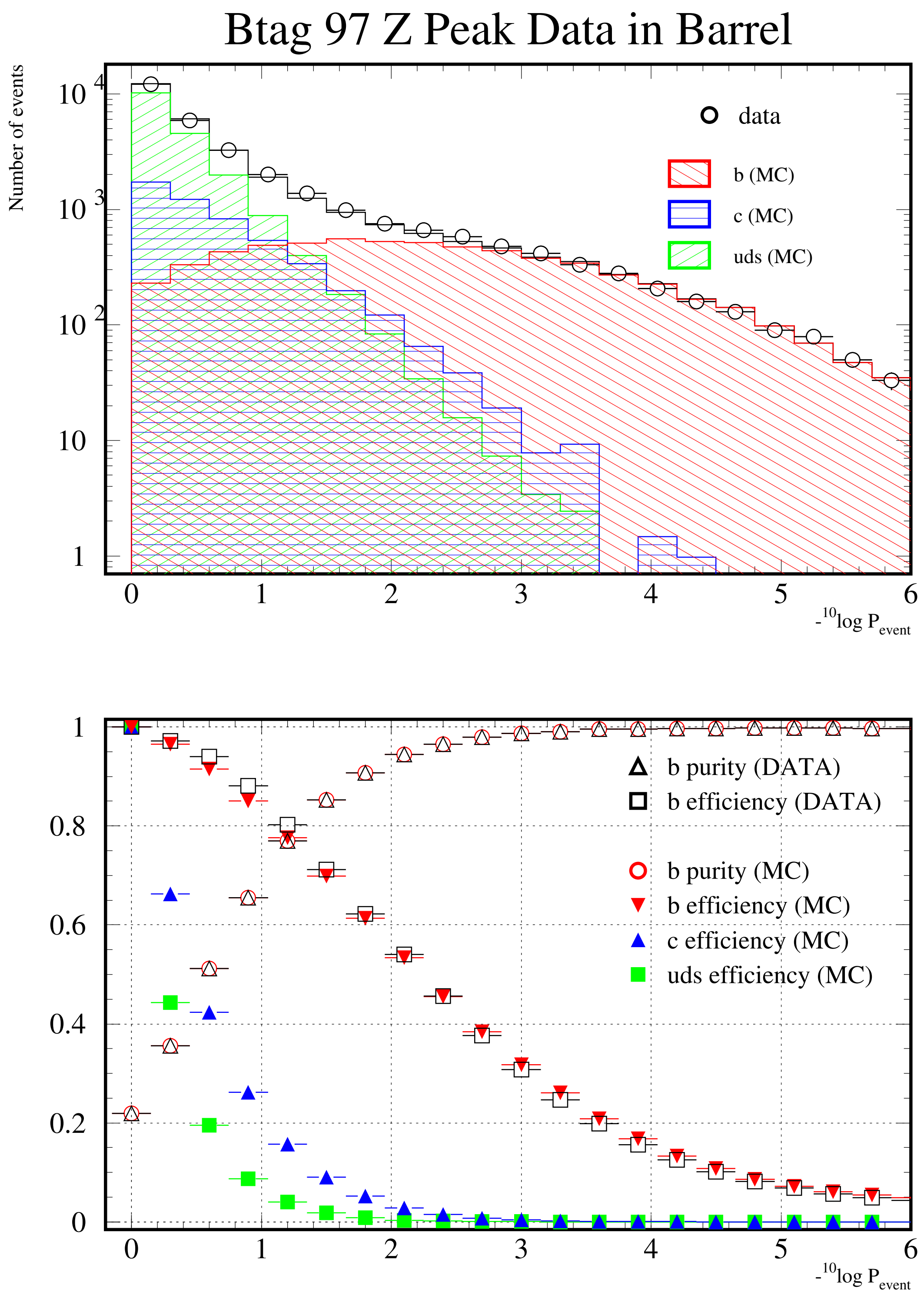

Figure 1: (a) The spectrum of the $B_{\rm tag}$ variable for the sample of $\mathrm{Z} \to \mathrm{q\bar{q}}$ events at 91 GeV. (b) The purity of the sample and the efficiency for $\mathrm{Z} \to \mathrm{b\bar{b}}$ events are presented as functions of the cut on the $B_{\rm tag}$ variable.

identification of b hadrons plays an especially important role. Both analyses proceed in the three stages outlined above.

First, a high multiplicity hadronic event preselection common to both channels is made at each center-of-mass energy. At least 15 tracks and 45 calorimetric clusters are required and the visible energy, E_{vis}, must exceed $0.6 \cdot \sqrt{s}$. Other preselection cuts which depend on the center-of-mass energy are shown in Table 1. Events passing the preselection are then forced to have four jets using the DURHAM [30] clustering algorithm and a kinematic fit requiring 4-momentum conservation (4C) is performed.

$\sqrt{s}$(GeV)	$\frac{E_{\mathrm{vis}}}{\sqrt{s}}$	N_{clus}	N_{trk}	$\frac{P_{\parallel}^{\mathrm{miss}}}{E_{\mathrm{vis}}}$	$\frac{P_{\perp}^{miss}}{E_{\mathrm{vis}}}$	$\sqrt{\frac{s'}{s}}$	$\frac{E_{\gamma}}{\sqrt{s}}$	Y_{34}^{D}
130	$\geq 0.6, \leq 1.4$	≥ 45	≥ 15	≤ 0.6	≤ 0.6	≥ 0.85	≤ 0.1	≥ 0.002
136	$\geq 0.6, \leq 1.4$	≥ 45	≥ 15	≤ 0.6	≤ 0.6	≥ 0.85	≤ 0.1	≥ 0.002
161	$\geq 0.6, \leq 2.0$	≥ 45	≥ 15	≤ 0.6	≤ 0.3	≥ 0.70	≤ 0.1	≥ 0.002
172	$\geq 0.6, \leq 1.4$	≥ 45	≥ 15	≤ 0.6	≤ 0.3	≥ 0.70	≤ 0.1	≥ 0.0005
183	$\geq 0.6, \leq 1.4$	≥ 45	≥ 15	≤ 0.4	≤ 0.3	≥ 0.80	≤ 0.1	≥ 0.002

Table 1: Preselection cuts for $\mathrm{hA} \to \mathrm{b\bar{b}b\bar{b}}$ and $\mathrm{hZ} \to \mathrm{b\bar{b}q\bar{q}}$ analyses at all center-of-mass energies. $E_{\mathrm{vis}}$is the visible energy; N_{clus} is the number of calorimetric clusters; N_{trk} is the number of tracks; $P_{\parallel}^{\mathrm{miss}}$and $P_{\perp}^{\mathrm{miss}}$ are the missing momentum parallel and perpendicular to the beam axis; $\sqrt{s'}$ is the effective center-of-mass energy [31] ; E_{γ} is the maximum energy of a photon in the detector; $Y_{34}^{\mathrm{D}}$is the Y_{cut} parameter where the event goes from a three-jets to a four-jets configuration in the DURHAM scheme.

The second stage of the analyses involves optimizing a set of cuts that maximizes the average confidence level to exclude the signal assuming the presence of only background using the technique described in reference [28]. In the $\mathrm{hZ} \to \mathrm{b\bar{b}q\bar{q}}$ selection, Y_{34}^{D}(the Y_{cut} in the DURHAM scheme where the event goes from a three-jets to a four-jets configuration) and the minimum dijet mass, $\min(M_i)$, are the two most important kinematics cuts, whereas in the $\mathrm{hA} \to \mathrm{b\bar{b}b\bar{b}}$ analysis, the $B_{\mathrm{tag}}^{\mathrm{event}}$ and the mass variable, χ_{hA} (see Equation 1), play a more important role. These variables are shown in Figure 2 for the data and Monte Carlo after the preselection but before the optimized cuts have been applied. The full list of variables with optimized cuts for $\mathrm{hA} \to \mathrm{b\bar{b}b\bar{b}}$ and $\mathrm{hZ} \to \mathrm{b\bar{b}q\bar{q}}$ at all the center-of-mass energies can be found in Table 2. The number of accepted events after the preselection and after passing either set of the optimized cuts (except the cut on the mass variable) for $\mathrm{hZ} \to \mathrm{b\bar{b}q\bar{q}}$ or $\mathrm{hA} \to \mathrm{b\bar{b}b\bar{b}}$ are shown in Table 3 for the data, Monte Carlo background and signal efficiency.

The following mass variables are defined:

$$\chi_{\mathrm{hA}} = \log\left(\mathrm{Prob}\left(\min\left((\Sigma_i - (m_{\mathrm{A}} + m_{\mathrm{H}}))^2 w_{\Sigma} + (\Delta_i - |m_{\mathrm{A}} - m_{\mathrm{H}}|)^2 w_{\Delta}\right)\right)\right) \quad (1)$$

$$\chi_{\mathrm{hZ}} = \log\left(\mathrm{Prob}\left(\min\left((\Sigma_i - (m_{\mathrm{Z}} + m_{\mathrm{H}}))^2 w_{\Sigma} + (\Delta_i - |m_{\mathrm{Z}} - m_{\mathrm{H}}|)^2 w_{\Delta}\right)\right)\right) \quad (2)$$

where Σ_i and Δ_i are the sum and difference, respectively, of the i^{th} dijet masses of one the three unique jet pairings. The weights w_{Σ} and w_{Δ} are respectively $1/(4\ \mathrm{GeV})^2$ and $1/(6\ \mathrm{GeV})^2$, and Prob is the probability of a χ^2 with two degrees of freedom.

Events passing the optimized cuts are then classified into categories: 1) those that pass only the hZ cuts; 2) those that pass only the hA cuts; and 3) those that pass both sets of cuts. Category (1) is called the $\mathrm{hZ}_{\mathrm{b\bar{b}q\bar{q}}}$ analysis and category (2) the $\mathrm{hA}_{\mathrm{b\bar{b}b\bar{b}}}$ analysis. Events

$\sqrt{s}$(GeV)	$\frac{M_i}{\sqrt{s}}$	$\frac{\min(E_{\rm jet})}{\sqrt{s}}$	$\frac{\max(\Delta E_{\rm jet})}{\sqrt{s}}$	$Y_{34}^{\rm D}$	$\frac{E_{\rm vis}}{\sqrt{s}}$	$\frac{P_{\parallel}^{\rm miss}}{E_{\rm vis}}$	$\chi_{\rm mass}$	$B_{\rm tag}^{\rm event}$
				$\rm hZ \rightarrow b\bar{b}q\bar{q}$				
161	$\geq 0.16, \leq 0.74$	≥ 0.09	≤ 0.36	≥ 0.0067	≥ 0.75	≤ 0.21	–	≥ 0.68
172	$\geq 0.13, \leq 0.72$	≥ 0.08	≤ 0.35	≥ 0.0034	≥ 0.66	≤ 0.18	≥ -16.0	≥ 0.16
183	$\geq 0.14, \leq 0.66$	≥ 0.12	≤ 0.22	≥ 0.0044	≥ 0.70	≤ 0.26	≥ -13.3	≥ 0.06
				$\rm hA \rightarrow b\bar{b}b\bar{b}$				
130	$\geq 0.14, \leq 0.82$	≥ 0.08	≤ 0.36	≥ 0.0079	≥ 0.70	≤ 0.22	≥ -7.0	≥ 0.32
136	$\geq 0.14, \leq 0.80$	≥ 0.06	≤ 0.36	≥ 0.0051	≥ 0.64	≤ 0.23	≥ -6.3	≥ 0.95
161	$\geq 0.00, \leq 0.77$	≥ 0.03	≤ 0.36	≥ 0.0025	≥ 0.65	≤ 0.23	≥ -10.2	≥ 0.87
172	$\geq 0.11, \leq 0.83$	≥ 0.01	≤ 0.38	≥ 0.0010	≥ 0.62	≤ 0.24	≥ -9.7	≥ 0.90
183	$\geq 0.09, \leq 0.78$	≥ 0.08	≤ 0.32	≥ 0.0030	≥ 0.65	≤ 0.21	≥ -6.1	≥ 0.67

Table 2: Optimized cuts for the $\rm hZ \rightarrow b\bar{b}q\bar{q}$ and $\rm hA \rightarrow b\bar{b}b\bar{b}$ analyses. If any of these variables fail the cuts listed, the event is rejected. M_i is the $i^{\rm th}$ dijet mass out of the three possible unique jet pairings. $\min(E_{\rm jet})$ is minimum jet energy. $\max(\Delta E_{\rm jet})$ is the maximum energy difference between any two jets. $Y_{34}^{\rm D}$ is the $Y_{\rm cut}$ parameter in the DURHAM scheme where the event changes from a three-jets to a four-jets configuration. $E_{\rm vis}$ is the visible energy. $P_{\parallel}^{\rm miss}$ is the missing momentum parallel to the beam axis. $\chi_{\rm mass}$ is the mass χ^2 parameter in the hZ mass hypothesis ($\chi_{\rm hZ}$) or hA mass hypothesis ($\chi_{\rm hA}$) depending on the analysis (see Equation 1 and 2) and $B_{\rm tag}^{\rm event}$is the event b-tag.

$\sqrt{s}$(GeV)	Preselection				Optimized Cuts $\rm hA_{b\bar{b}b\bar{b}}$or $\rm hZ_{b\bar{b}q\bar{q}}$			
	$\epsilon_{\rm hA\rightarrow b\bar{b}b\bar{b}}$	$\epsilon_{\rm hZ\rightarrow b\bar{b}q\bar{q}}$	$N_{\rm bg}$	$N_{\rm data}$	$\epsilon_{\rm hA\rightarrow b\bar{b}b\bar{b}}$	$\epsilon_{\rm hZ\rightarrow b\bar{b}q\bar{q}}$	$N_{\rm bg}$	$N_{\rm data}$
130	0.921	–	148.9	148	0.663	–	20.1	19
136	0.921	–	112.0	118	0.699	–	9.5	11
161	0.936	0.949	134.5	128	0.847	0.747	25.2	14
172	0.954	0.970	193.7	186	0.833	0.889	84.0	80
183	0.887	0.913	655.6	652	0.780	0.836	380.5	376

Table 3: Analysis flow. On the left hand side are the number of observed data, $N_{\rm data}$, expected background, $N_{\rm bg}$, and signal efficiencies for events passing the common hA and hZ preselection. On the right hand side, the same is shown for events passing either set of the optimized cuts found in Table 2. The signal efficiencies, $\epsilon_{\rm hA\rightarrow b\bar{b}b\bar{b}}$, are for the following signal masses: 130-136 GeV, $m_{\rm A}$=$m_{\rm H}$=50 GeV; 161-172 GeV, $m_{\rm A}$=$m_{\rm H}$=60 GeV; 183 GeV, $m_{\rm A}$=$m_{\rm H}$=70 GeV. The efficiencies, $\epsilon_{\rm hZ\rightarrow b\bar{b}q\bar{q}}$, are for: 161-172 GeV, $m_{\rm H}$=71 GeV; 183 GeV, $m_{\rm H}$=85 GeV. At this stage of the analysis, the acceptances are independent of $\tan\beta$.

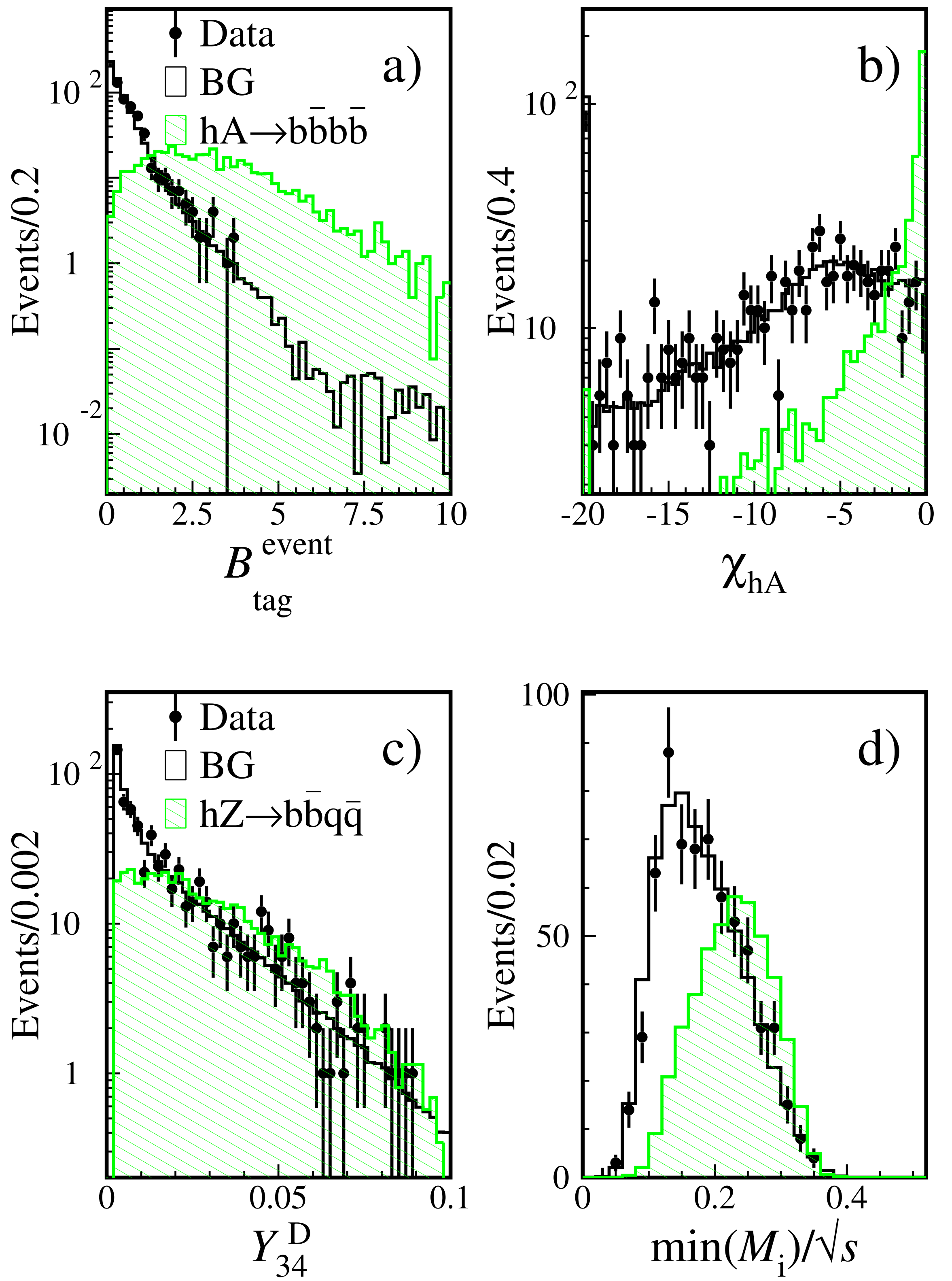

Figure 2: The most important optimized cuts in the hA $\to$ b$\overline{\text{b}}$b$\overline{\text{b}}$ and hZ $\to$ b$\overline{\text{b}}$q$\overline{\text{q}}$ analyses. In the plots, the points are data, the solid histograms are the Monte Carlo backgrounds and the superimposed hatched histograms are the hA or hZ signals normalized to efficiency x 500. The distributions are shown after preselection, but before optimized cuts: **a)** Event b-tag, $B_{\text{tag}}^{\text{event}}$for the hA $\to$ b$\overline{\text{b}}$b$\overline{\text{b}}$ analysis; **b)** Mass variable, χ_{mass}, for the hA $\to$ b$\overline{\text{b}}$b$\overline{\text{b}}$ analysis at $\tan\beta = 1$, $m_{\text{H}} = 85$ GeV, typical mixing; **c)** $Y_{34}^{\text{D}}$for the hZ $\to$ b$\overline{\text{b}}$q$\overline{\text{q}}$analysis; **d)** Minimum, normalized dijet mass, $\min(M_i/\sqrt{s})$ for the hZ $\to$ b$\overline{\text{b}}$q$\overline{\text{q}}$ analysis at $\tan\beta = 55$, $m_{\text{A}} = m_{\text{H}} = 70$ GeV, typical mixing.

in category (3), however, are split into two separate analyses by choosing the most likely production hypothesis based on the probability of the χ^2 of the mass hypothesis and the relative production rates. If $\sigma_{\mathrm{hA}\rightarrow\mathrm{b\bar{b}b\bar{b}}} \cdot \mathrm{Prob}(\chi^2(m_{\mathrm{A}}, m_{\mathrm{H}})) > \sigma_{\mathrm{hZ}\rightarrow\mathrm{b\bar{b}q\bar{q}}} \cdot \mathrm{Prob}(\chi^2(m_{\mathrm{Z}}, m_{\mathrm{H}}))$, then the event is classified as $\mathrm{hA} \rightarrow \mathrm{b\bar{b}b\bar{b}}$ and this analysis is called $\mathrm{hA}'_{\mathrm{b\bar{b}b\bar{b}}}$, otherwise it is classified as $\mathrm{hZ} \rightarrow \mathrm{b\bar{b}q\bar{q}}$ and called $\mathrm{hZ}'_{\mathrm{b\bar{b}q\bar{q}}}$.

In the last stage of the $\mathrm{hZ}_{\mathrm{b\bar{b}q\bar{q}}}$, $\mathrm{hA}_{\mathrm{b\bar{b}b\bar{b}}}$, $\mathrm{hZ}'_{\mathrm{b\bar{b}q\bar{q}}}$ and $\mathrm{hA}'_{\mathrm{b\bar{b}b\bar{b}}}$ analyses, the discriminating variables, $F(m_{\mathrm{Z}}, m_{\mathrm{H}})$ and $F(m_{\mathrm{A}}, m_{\mathrm{H}})$, are computed. These variables are the weighted combination of the $B_{\mathrm{tag}}^{\mathrm{event}}$ and χ probabilities:

$$F = -\log\left(\frac{\omega P_B^{1/\omega} P_\chi - P_B P_\chi^\omega}{\omega - 1}\right), \tag{3}$$

where P_B and P_χ are the probabilities of $B_{\mathrm{tag}}^{\mathrm{event}}$and χ each being consistent with their respective background distributions, and ω is a weighting parameter that is optimized for each analysis. For the $\mathrm{hZ}_{\mathrm{b\bar{b}q\bar{q}}}$and $\mathrm{hZ}'_{\mathrm{b\bar{b}q\bar{q}}}$analyses, the mass variable $\chi = \chi_{\mathrm{hZ}}$ is used and F is a function of the m_{H}hypothesis, $F(m_{\mathrm{Z}}, m_{\mathrm{H}})$. Conversely, for $\mathrm{hA}_{\mathrm{b\bar{b}b\bar{b}}}$ and $\mathrm{hA}'_{\mathrm{b\bar{b}b\bar{b}}}$ $\chi = \chi_{\mathrm{hA}}$ is used and F depends on the m_{A} and m_{H} mass hypothesis, $F(m_{\mathrm{A}}, m_{\mathrm{H}})$. Spectra of $F(m_{\mathrm{A}}, m_{\mathrm{H}})$ and $F(m_{\mathrm{Z}}, m_{\mathrm{H}})$ for the $\sqrt{s}$= 183 GeV analyses can be seen in Figures 3a and 3b, for the $\mathrm{hA}_{\mathrm{b\bar{b}b\bar{b}}}$ and $\mathrm{hA}'_{\mathrm{b\bar{b}b\bar{b}}}$ analyses for a mass hypothesis of $m_{\mathrm{A}} = m_{\mathrm{H}} = 70$ GeV, and in Figures 3c and 3d, for the $\mathrm{hZ}_{\mathrm{b\bar{b}q\bar{q}}}$ and $\mathrm{hZ}'_{\mathrm{b\bar{b}q\bar{q}}}$ analyses for the $m_{\mathrm{H}} = 85$ GeV mass hypothesis in the typical mixing scheme.

The $\mathrm{hA} \rightarrow \tau^+\tau^-\ \mathrm{b\bar{b}}$, $\mathrm{hZ} \rightarrow \tau^+\tau^-\ \mathrm{b\bar{b}}$ and $\mathrm{hZ} \rightarrow \mathrm{q\bar{q}}\,\tau^+\tau^-$ channels

The signatures of these events are a pair of high energy taus accompanied by two hadronic jets. The identification criteria of hadronically and leptonically decaying taus are given in [32].

An automated procedure [29] is used to optimise the selection criteria. The optimisation is done independently at all the centre–of–mass energies. The optimised values of the cuts are rounded to 3–4 significant digits. At first, high multiplicity events are requested asking for a number of tracks (N_{gtk}) greater than 5 and a number of calorimetric clusters (N_{cl}) greater than 15. Then, cuts on the visible energy (E_{vis}) and the visible mass (M_{vis}) of the event are applied. Finally, two taus are required (allowing both hadronically and leptonically decaying taus). Energy cuts are then applied on the two selected leptons, differently for the most or least energetic and depending on the lepton type ($E_{min}^{l,j}, l = e, \mu, \tau, j = 1, 2$). The isolation criteria for electrons and muons consider the number of tracks in a 20^0 cone around the electron one, N_{20}^t, and the number of clusters between 5^0 and 20^0, around a muon, $N_{20/5}^c$. The selected hadronically decaying τ candidates have to fulfill some isolation requirements mainly to reject the $\mathrm{Z}/\gamma^* \rightarrow \mathrm{q\bar{q}}$ and the $\mathrm{WW} \rightarrow$ four jets background: a low number of tracks in a 10^0 cone around the τ (N_{10}^t) and a low ratio of the energies deposited in a 30^0 and 10^0 cones ($\frac{E_{30/10}}{E_{10}}$). To further reduce the background from radiative return to the Z events, a cut on the $\sqrt{s'}$ is applied. Moreover, to reduce the contribution due to semileptonic decays of the W, a cut on the sum of the maxima energy of the two identified leptons and the missing energy of the events (Σ_{lm}) is applied. Once the two leptons are selected, the rest of the event is forced in two jets and the di–jet and di–tau invariant masses (M_{jj} and $M_{\tau\tau}$ respectively) are built. Four–momentum conservation constraints are applied in the kinematic fit to improve the invariant mass resolution. To reduce the background, each mass is required to be in a reasonable large mass interval (according to the choosen mass points): 30 GeV $\leq M_{jj}$, $M_{\tau\tau} \leq 120$ GeV and 50 GeV $\leq M_{jj} + M_{\tau\tau} \leq 220$ GeV.

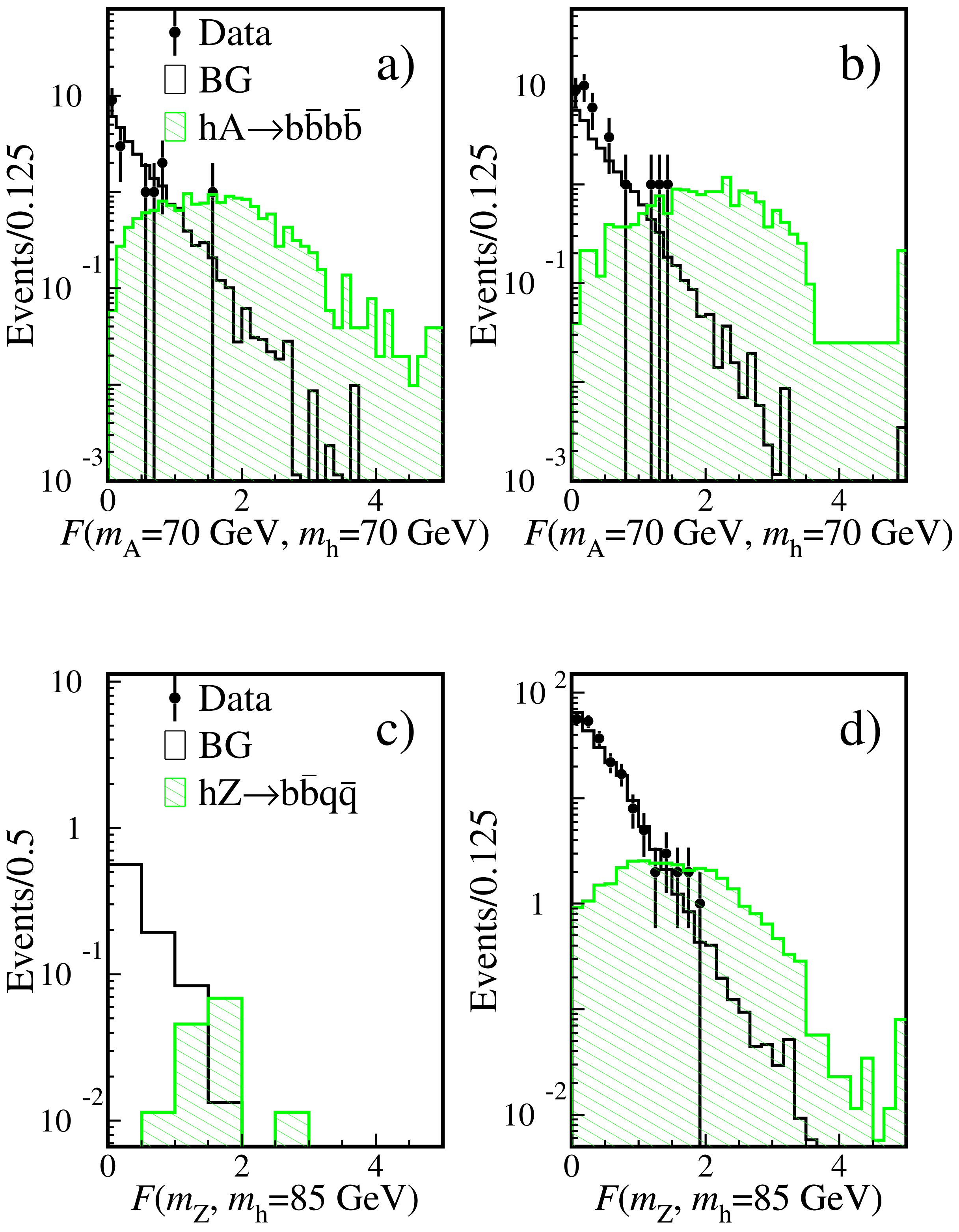

Figure 3: The discriminant, $F(m_{\mathrm{A}}, m_{\mathrm{H}})$, for the two most important $\mathrm{hA} \rightarrow \mathrm{b\bar{b}b\bar{b}}$ analyses and $F(m_{\mathrm{Z}}, m_{\mathrm{H}})$ for the two most important $\mathrm{hZ} \rightarrow \mathrm{b\bar{b}q\bar{q}}$ analyses after the optimized cuts have been applied. Data are the points, the open histograms are Monte Carlo background and the superimposed hatched histograms are signal efficiency x 50: **a,b)** $\mathrm{hA_{b\bar{b}b\bar{b}}}$ and $\mathrm{hA'_{b\bar{b}b\bar{b}}}$ analyses at $\tan\beta = 55$, $m_{\mathrm{A}} = m_{\mathrm{H}} = 70$ GeV, typical mixing; **c,d** $\mathrm{hZ_{b\bar{b}q\bar{q}}}$ and $\mathrm{hZ'_{b\bar{b}q\bar{q}}}$ analyses at $\tan\beta = 1$, $m_{\mathrm{H}} = 85$ GeV, typical mixing.

All the cuts, except the ones on the number of tracks and clusters and on the invariant masses, are automatically optimised. The optimised cuts at the four centre–of–mass energies are shown in Table 4. The number of data and expected background events are shown in Table 5. The efficiencies for the neutral–pair are shown in Table 6 for several Higgs masses. The efficiencies for the Higgs–strahlung process are shown in Table 7.

After the optimized selection, the final discriminating variable to distinguish signal from background is built. The events passing the common set of optimized cuts are classified as either $\mathrm{hA} \to \mathrm{b\bar{b}}\tau^+\tau^-(\tau^+\tau^-\mathrm{b\bar{b}})$, $\mathrm{hZ} \to \mathrm{b\bar{b}}\tau^+\tau^-$ or $\mathrm{hZ} \to \tau^+\tau^-\mathrm{q\bar{q}}$ by choosing the most likely production hypothesis based on the mass χ^2 variables and the relative production rates as in the $\mathrm{hA} \to \mathrm{b\bar{b}b\bar{b}}$ and $\mathrm{hZ} \to \mathrm{b\bar{b}q\bar{q}}$ analyses. The mass χ^2 variables are defined as in Equation 1 but with the weights $1/(5\ \mathrm{GeV})^2$ and $1/(10\ \mathrm{GeV})^2$ for the sum and difference of M_i and M_τ. The mass-dependent variable, $\mathcal{P} = 10^{-F}$, is defined using Equation 3 for the case of a weight of unity, which reduces to $F = -\log(P_B P_\chi(1 - \ln(P_B P_\chi)))$. Here, P_B and P_χ are the confidence levels that the $B_{\mathrm{tag}}^{\mathrm{event}}$ (from the two hadronic jets) and mass χ^2 are consistent with their signal distributions. In the case of the $\mathrm{hZ} \to \tau^+\tau^-\mathrm{q\bar{q}}$ analysis, the b-tagging information is not used and $F = -\log P_\chi$. The event is classified depending on the value of

$$\mathcal{P} = \max(\sigma_{\mathrm{hA}\to\mathrm{b\bar{b}}\tau^+\tau^-(\tau^+\tau^-\mathrm{b\bar{b}})}\cdot\mathcal{P}(m_\mathrm{A}, m_\mathrm{H}), \sigma_{\mathrm{hZ}\to\mathrm{b\bar{b}}\tau^+\tau^-}\cdot\mathcal{P}(m_\mathrm{Z}, m_\mathrm{H}), \sigma_{\mathrm{hZ}\to\tau^+\tau^-\mathrm{q\bar{q}}}\cdot\mathcal{P}(m_\mathrm{Z}, m_\mathrm{H}))/\sigma_{\mathrm{b}\tau}$$

where $\sigma_{\mathrm{b}\tau}$ is the sum of these three cross sections.

Unlike the $\mathrm{hA} \to \mathrm{b\bar{b}b\bar{b}}$ and $\mathrm{hZ} \to \mathrm{b\bar{b}q\bar{q}}$ analyses, the events are not split into separate categories based on this decision, but are instead kept as one inclusive analysis. The discriminant, $\mathcal{P}$, is recalculated at each $(\tan\beta, m_\mathrm{A})$ point in the scan for each mixing scenario. The spectrum for $\mathcal{P}$ at $(\tan\beta = 50, m_\mathrm{A} = 70\ \mathrm{GeV})$ is shown in Figure 4 for the 183 GeV data, Monte Carlo background and an inclusive signal of $\mathrm{hA} \to \mathrm{b\bar{b}}\tau^+\tau^-(\tau^+\tau^-\mathrm{b\bar{b}}) + \mathrm{hZ} \to \mathrm{b\bar{b}}\tau^+\tau^- + \mathrm{hZ} \to \tau^+\tau^-\mathrm{q\bar{q}}$ in the minimal mixing scenario. In Figure 5, the number of the expected events in background and signal and number of data observed as a function of the step of cut on the final distribution $\mathcal{P}$ and the cumulative distribution for background and data are shown. In all the plots the three channels are summed together.

Systematic errors

Detector efficiencies and backgrounds for all the channels are estimated from the Monte Carlo simulation. Uncertainties on these estimates are treated as Gaussian and, for a single channel, assumed to be independent. The correlations between the channels and different centre-of-mass energies are accounted for in the final result.

Experimental uncertainties in the LEP centre-of-mass energy of ± 0.03 GeV [33] and in the luminosity measurements account for 1% systematic error on the number of expected signal events. Theoretical errors on the Higgs boson production cross section and branching ratios due to the uncertainties in α_s [34] ($\sim 0.1\%$), interference effects [35] ($\sim 1\%$) and quark masses [36] ($\sim 1\%$) introduce an additional uncertainty on the predicted number of signal events.

Studies of the possible systematic effects due to the topological cuts are described in detail in [37] for the four-jet channel. Similar studies are performed for the other channels. The net effect on the number of expected signal events is found to be 1% with almost equal contributions from tracking efficiency and uncertainty in the absolute energy scale. The systematic uncertainty due to the B-tagging is estimated using the calibration sample of hadronic events at 91 GeV and assuming that the difference between data and Monte Carlo distributions is entirely due to the systematic effects. The effect on the signal efficiency is evaluated to be $3 - 5\%$, depending

cut		$\sqrt{s} = 133$ GeV	$\sqrt{s} = 161$ GeV	$\sqrt{s} = 172$ GeV	$\sqrt{s} = 183$ GeV
$\frac{E_{\text{vis}}}{\sqrt{s}}$	$>$	0.3210	0.4060	0.3190	0.3710
$\frac{E_{\text{vis}}}{\sqrt{s}}$	$<$	1.1200	0.9740	1.0900	1.0300
$\frac{M_{\text{vis}}}{\sqrt{s}}$	$>$	0.3120	0.4480	0.4350	0.4750
$\frac{M_{\text{vis}}}{\sqrt{s}}$	$<$	1.9500	1.0300	1.0700	1.0800
$\sqrt{\frac{s'}{s}}$	$>$	0.4040	0.6250	0.5500	0.5960
Σ_{lm} (GeV)	$<$	120.0000	57.1000	70.4000	60.0000
$E^{e,2}_{min}$ (GeV)	$>$	3.0100	3.0200	3.0700	3.3600
$E^{\mu,2}_{min}$(GeV)	$>$	3.0200	3.8600	3.0100	3.0100
$E^{\tau,2}_{min}$(GeV)	$>$	3.0100	3.0300	3.1400	3.1500
$E^{e,1}_{min}$ (GeV)	$>$	3.0100	3.0100	3.0100	3.1900
$E^{\mu,1}_{min}$(GeV)	$>$	3.0300	3.0100	3.0100	3.0200
$E^{\tau,1}_{min}$(GeV)	$>$	3.4300	3.4300	4.2800	5.9800
N^t_{20}	$<$	4.7800	4.0500	2.1800	4.2100
$N^c_{20/5}$	$<$	5.9700	3.0000	5.7500	3.1100
N^t_{10}	$<$	6.9900	6.9800	6.9900	6.8600
$\frac{E_{30/10}}{E_{10}}$	$<$	0.2980	0.2930	0.2980	0.2940

Table 4: The optimised sets of cuts at the different centre–of–mass energies for the tau–channels.

	$\sqrt{s} = 133$ GeV	$\sqrt{s} = 161$ GeV	$\sqrt{s} = 172$ GeV	$\sqrt{s} = 183$ GeV
Background	2.7	1.8	4.1	14.0
Data	4	2	3	17

Table 5: Number of data and expected background events in the tau channels.

Signal efficiencies (%)				
m_{h}(GeV); m_{A}(GeV)	$\sqrt{s} = 133$ GeV	$\sqrt{s} = 161$ GeV	$\sqrt{s} = 172$ GeV	$\sqrt{s} = 183$ GeV
50;50	27.0	31.1	34.1	30.0
50;60	25.3	31.8	31.6	29.0
50;70	27.0	33.3	34.6	32.5
50;80	–	31.2	34.0	–
50;90	–	31.6	32.7	–
50;100	–	30.1	32.7	–
50;110	–	28.3	29.3	–
60;60	28.1	31.7	33.0	29.7
60;70	29.1	28.9	34.1	31.8
60;80	–	31.3	34.9	29.8
60;90	–	28.3	33.0	–
60;100	–	31.7	30.5	–
60;110	–	–	27.7	–
70;70	–	28.3	33.4	32.3
70;80	–	30.2	30.3	32.9
70;90	–	30.1	29.5	–
70;100	–	–	26.7	25.2
80;80	–	28.9	29.5	29.5
80;90	–	–	30.2	–

Table 6: Signal efficiencies for neutral–pair production in the tau channels.

Signal efficiencies (%)			
$\tau^+\tau^-\mathrm{b\bar{b}}$ Channel			
m_{h}(GeV)	$\sqrt{s} = 161$ GeV	$\sqrt{s} = 172$ GeV	$\sqrt{s} = 183$ GeV
60	26.7	24.3	26.4
70	30.3	23.5	29.7
80	23.8	20.2	25.6
85	–	–	25.3
90	–	–	25.8
$\mathrm{q\bar{q}}\tau^+\tau^-$ Channel			
m_{h}(GeV)	$\sqrt{s} = 161$ GeV	$\sqrt{s} = 172$ GeV	$\sqrt{s} = 183$ GeV
60	24.6	23.2	26.9
70	26.8	23.6	29.4
80	28.4	20.4	28.1
85	–	–	28.6
90	–	–	29.7

Table 7: Signal efficiencies for Higgs–strahlung production in the tau channels.

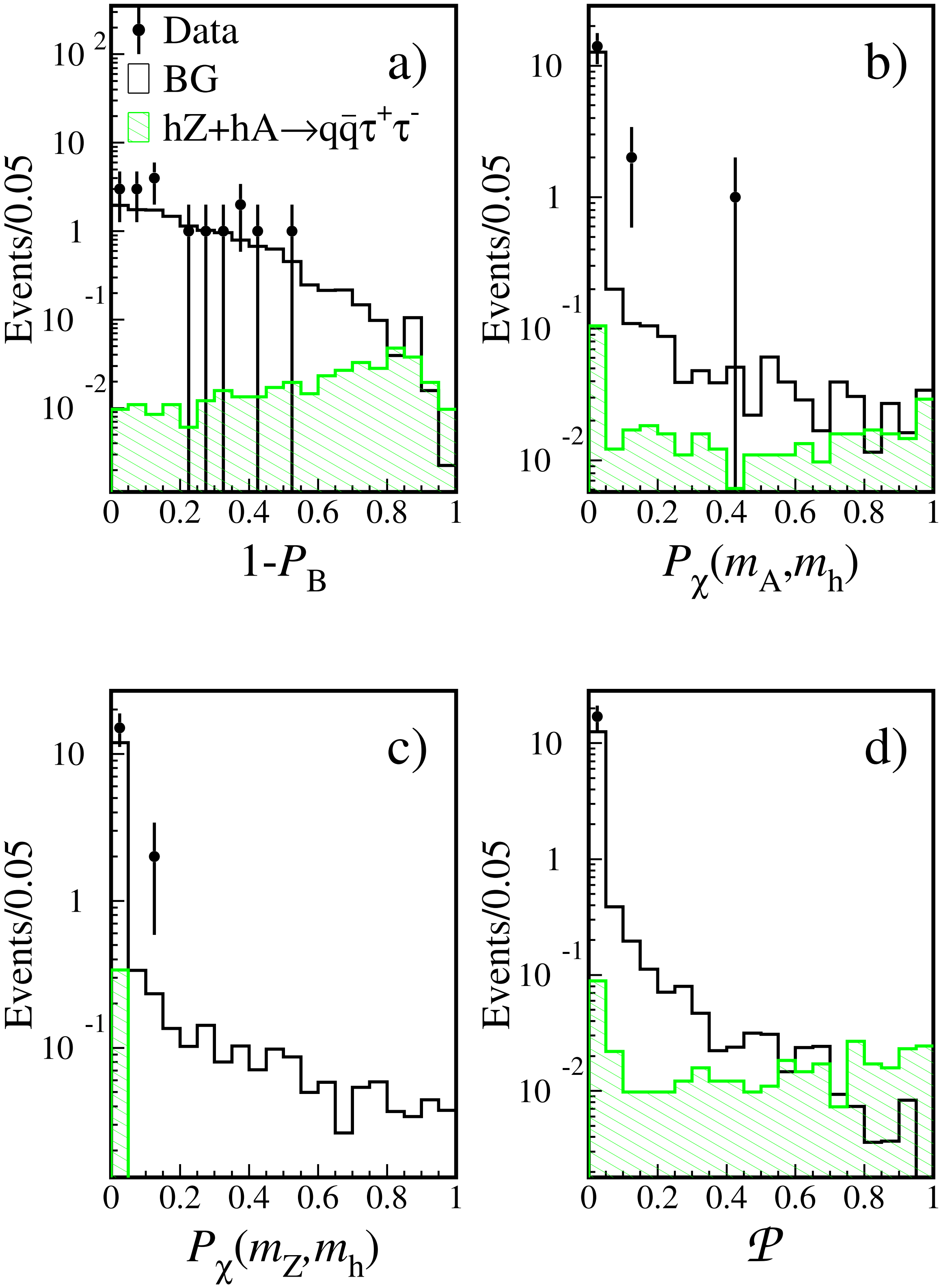

Figure 4: Construction of $\mathcal{P}$, for the hA $\rightarrow$ b$\overline{\rm b}\tau^+\tau^-(\tau^+\tau^-b\bar{\rm b})$, hZ $\rightarrow$ b$\overline{\rm b}\tau^+\tau^-$ and hZ $\rightarrow \tau^+\tau^-$q$\overline{\rm q}$ analyses at 183 GeV for $(\tan\beta = 50, m_{\rm A} = 70$ GeV$)$ for minimal mixing $(\sigma_{\rm hA} = 0.148$ pb;$\sigma_{\rm hZ} = 0.0017$ pb$)$. The dots are data, the solid histogram is Monte Carlo and the hatched histogram is the inclusive signal hA $\rightarrow$ b$\overline{\rm b}\tau^+\tau^-(\tau^+\tau^-b\bar{\rm b})$ + hZ $\rightarrow$ b$\overline{\rm b}\tau^+\tau^-$ + hZ $\rightarrow \tau^+\tau^-$q$\overline{\rm q}$. **a)** The $B_{\rm tag}^{\rm event}$probability to be signal. **b)** The mass probability to be signal. **c)** The mass probability for the hZ mass hypothesis. **d)** The discriminant, $\mathcal{P}$, for the inclusive b$\bar{\rm b}\tau^+\tau^-$ analysis.

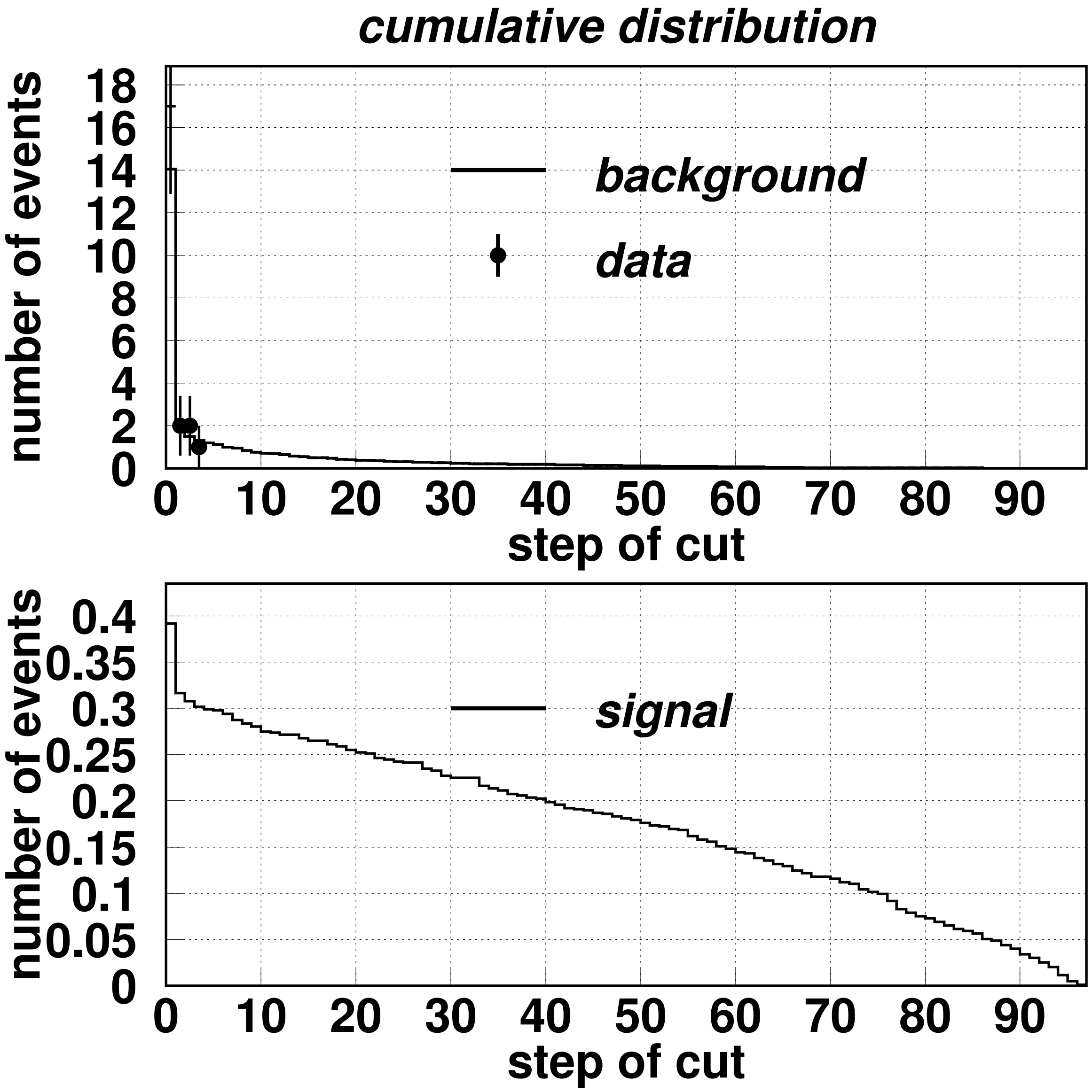

Figure 5: Cumulative distribution. The number of the expected events in background and signal and number of data observed as a function of the step of cut on the final distribution $\mathcal{P}$ at $\tan\beta = 50; m_{\rm A} = 70$ GeV; $\sigma_{\rm hA} = 0.148$ pb; $\sigma_{\rm hZ} = 0.0017$ pb.

on the channel, by reweighting the signal distributions accordingly. The Monte Carlo statistics adds 2% to the error on the signal efficiency. Assuming these uncertainties are independent, the overall systematic error on the number of signal events is estimated to be 4%.

The uncertainty on the background mainly comes from two different sources: Monte Carlo statistics and the normalisation error due to the uncertainty on both the cross section and the selection efficiency for the background processes. The error from the Monte Carlo statistics is relatively large but completely uncorrelated between the different bins of the individual channels; this fact leads to a negligible effect on the confidence level evaluation. The overall normalisation error is the most important and is estimated to be 10%. It is assumed to be fully correlated between the different channels.

Results

The final discriminant variable, F, which is used in the limit derivation, is recomputed at each $(\tan\beta, m_{\mathrm{A}})$ point in the scan for the mixing scenario under consideration. Because of the cut on the χ variables, the number of accepted data, Monte Carlo background and signal events changes at each scanned point. This can be seen in the inclusive signal efficiency for $\mathrm{hZ}+\mathrm{hA}$ production. In Figures 6a and 6b, the inclusive efficiency near the average 95% CL limit as well as the number of accepted data and background events is shown as a function of $\tan\beta$ for maximal mixing.

The limits on the Higgs bosons masses are derived according to different sets of MSSM parameters, as suggested in reference [38], which makes use of the the Grand Unification assumption (see reference [38]). This assumption has little impact on the phenomenology of the Higgs sector, but it reduces the number of free parameters in the MSSM. The free parameters are chosen to be the ratio of the two Higgs vacuum expectation values, $\tan\beta$; the pseudoscalar Higgs mass, m_{A}; the gaugino mass parameter, M_2; the scalar fermion mass, m_0; the squark mixing masses, A_t, A_b; and the Higgs mass parameter, μ. The three sets of MSSM parameters used in this letter are called "minimal mixing", where $A_t = A_b = 0$ TeV and $\mu = -0.1$ TeV; "typical mixing", $A_t = A_b = 1$ TeV and $\mu = -1$ TeV; and "maximal mixing", $A_t = A_b = \sqrt{6}$ TeV and $\mu = -0.1$ TeV. For all three mixing scenarios, the mass of the top quark, m_{t}, is taken to be $m_{\mathrm{t}}= 175$ GeV, and $M_2 = m_0 = 1$ TeV. Finally, a scan over the two remaining independent parameters, $\tan\beta$ and m_{A}, is performed in each mixing scheme for the ranges,

$$1 \leq \tan\beta \leq 50;$$

$$30 \text{ GeV} \leq m_{\mathrm{A}} \leq 1000 \text{ GeV}.$$

since they are the ranges where the investigated final states are by far the dominant decay modes. Studies of $m_{\mathrm{A}} \leq 30$ GeV are reported in references [39–47].

The results of the search are evaluated by calculating the confidence level (CL) that the expected signal is absent in the data observed for the plane defined by $\tan\beta$ and m_{H}. The CL is calculated using the technique described in reference [48]. The results of all the analyses performed for all physics processes and decay channels are combined into bins of one distribution ordered in the log of signal-over-background. The CL is calculated from this signal-over-background distribution. Bins of an analysis with a signal-over-background ratio of less than 0.10 are not considered in the calculation of CL. This cut is chosen to maximize the average CL in the presence of the systematic and statistical error corrections as calculated from a large set of Monte Carlo experiments. Two examples of the distribution of the signal-over-background

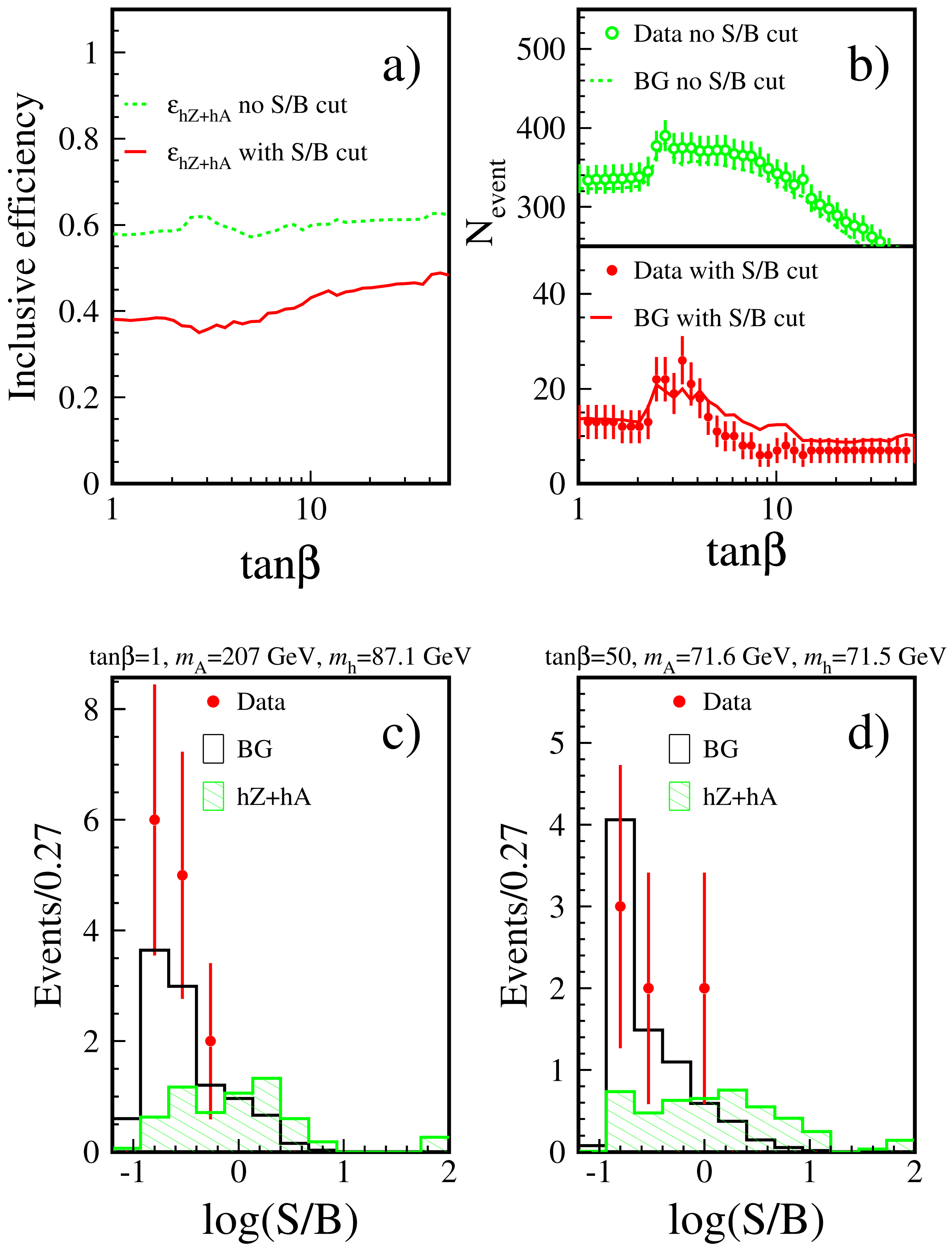

Figure 6: Accepted events and signal efficiency near the average 95% CL limit as a function of $\tan\beta$ for maximal mixing. **a)** Inclusive efficiency for hA + hZ production before a signal-over-background cut (dotted line) and after a signal-over-background cut of 0.1 (solid line). **b)** Upper plot: Number of accepted data events (dots) and expected background (dotted line) before a signal-over-background cut. Lower plot: Number of data events (dots) and background (solid line) passing a signal-over-background cut of 0.1. **c)** Signal-over-background distribution for all analyses combined in bins of log(Signal/Background) for $\tan\beta = 1, m_A = 207$ GeV, where hZ is the dominant physics channel (open histogram is expected background, dots are data, hatched histogram is combined signal). **d)** Same as **(c)**, but for $\tan\beta = 50, m_A = 71.6$ GeV, where hA is the dominant physics channel.

distribution for all analyses combined in bins of log(Signal/Background) for ($\tan\beta = 1, m_{\mathrm{A}} = 207$ GeV), where hZ is the dominant physics channel, and for ($\tan\beta = 50, m_{\mathrm{A}} = 71.6$ GeV), where hA is the dominant physics channel, are shown in Figures 6 c) and 6 d), respectively. The corresponding numbers of observed data, expected background and signal are shown in Table 8, where also the contributions from the different channels are reported.

		$\tan\beta = 1$ $m_{\mathrm{H}} = 87.1$ GeV			$\tan\beta = 50$ $m_{\mathrm{H}} = 71.5$ GeV		
Selection	$\sqrt{s}$ (GeV)	$\mathrm{N_{data}}$	$\mathrm{N_{bg}}$	$\mathrm{N_{sig}}$	$\mathrm{N_{data}}$	$\mathrm{N_{bg}}$	$\mathrm{N_{sig}}$
hA	183	0	0.0	0.0	1	2.6	1.4
hA	172	0	0.0	0.0	0	0.2	0.1
hA	161	0	0.0	0.0	0	0.2	0.0
$\mathrm{hA}'_{\mathrm{b\bar{b}b\bar{b}}}$	183	0	0.0	0.0	4	2.3	1.7
$\mathrm{hA}'_{\mathrm{b\bar{b}b\bar{b}}}$	172	0	0.0	0.0	1	1.0	0.5
$\mathrm{hA}'_{\mathrm{b\bar{b}b\bar{b}}}$	161	0	0.0	0.0	1	0.8	0.4
$\mathrm{hZ}'_{\mathrm{b\bar{b}q\bar{q}}}$	183	10	6.7	3.8	0	0.5	0.3
$\mathrm{hZ}'_{\mathrm{b\bar{b}q\bar{q}}}$	172	0	0.1	0.0	0	0.1	0.0
$\mathrm{hZ}'_{\mathrm{b\bar{b}q\bar{q}}}$	161	0	0.0	0.0	0	0.0	0.0
hZ	183	0	0.0	0.0	0	0.0	0.0
$\mathrm{hA} \to \mathrm{b\bar{b}}\tau^+\tau^-(\tau^+\tau^-\mathrm{b\bar{b}})$, $\mathrm{hZ} \to \mathrm{b\bar{b}}\tau^+\tau^-$, and $\mathrm{hZ} \to \tau^+\tau^-\mathrm{q\bar{q}}$	183	0	0.0	0.3	0	0.2	0.2
$\mathrm{hA} \to \mathrm{b\bar{b}}\tau^+\tau^-(\tau^+\tau^-\mathrm{b\bar{b}})$, $\mathrm{hZ} \to \mathrm{b\bar{b}}\tau^+\tau^-$, and $\mathrm{hZ} \to \tau^+\tau^-\mathrm{q\bar{q}}$	172	0	0.0	0.0	0	0.0	0.0
$\mathrm{hA} \to \mathrm{b\bar{b}}\tau^+\tau^-(\tau^+\tau^-\mathrm{b\bar{b}})$, $\mathrm{hZ} \to \mathrm{b\bar{b}}\tau^+\tau^-$, and $\mathrm{hZ} \to \tau^+\tau^-\mathrm{q\bar{q}}$	161	0	0.0	0.0	0	0.0	0.0
$\mathrm{hZ} \to \mathrm{q\bar{q}}\nu\bar{\nu}$	183	3	3.1	1.5	0	0.0	0.0
$\mathrm{hZ} \to \mathrm{q\bar{q}e^+e^-}$	183	0	0.2	0.3	0	0.0	0.0
$\mathrm{hZ} \to \mathrm{q\bar{q}}\mu^+\mu^-$	183	0	0.2	0.2	0	0.0	0.0
Total		13	10.3	6.1	7	7.9	4.7

Table 8: The number of observed data, expected background and signal for high and low $\tan\beta$ near the 95% CL for maximal mixing corresponding to Figures 6 c) and 6 d). For the 4–jet channel, where the analysis is split, all categories are listed separately. The signal is the sum of the hA and hZ contribution in each category. For the events involving taus an inclusive search is performed and the numbers given are for the four search channels combined. The 130 GeV and 136 GeV analyses are not listed in the table because their contribution at the limit is very small. The number of expected background and signal events are rounded to one significant digit after the decimal place.

Systematic and statistical errors on the signal and background are implemented in the CL calculation using the same procedure as in the Minimal Standard Model Higgs search [26].

The CL as a function of m_{H} and $\tan\beta$ is shown in Figure 7 for the different mixing hypotheses. No significant excess is observed at any point in the ($m_{\mathrm{H}}, \tan\beta$) plane for the three mixings.

Lower limits on the Higgs boson masses as a function of $\tan\beta$ are shown in Figure 7 for the different mixing hypotheses. The 95% CL lower mass limits on m_{A} and m_{H}, as well as the probability to obtain a limit on m_{H} larger than the one observed, are shown in Table 9 at the two extrema of the scan over $\tan\beta$. The lowest value of m_{H} excluded is at $\tan\beta = 20.3$ for typical mixing, and the lowest value of m_{A} excluded is at $\tan\beta = 22.4$ for minimal mixing. For the MSSM parameters considered this results in lower mass limits at the 95% CL of

$$\boldsymbol{m_{\mathrm{H}} > 70.7\ \mathrm{GeV}},$$

$$\boldsymbol{m_{\mathrm{A}} > 71.0\ \mathrm{GeV}}.$$

	N_{events} at 95% CL			Lower mass limits in GeV at 95% CL						
Mixing, $\tan\beta$	N_{bg}	N_{data}	N_{sig}	$\overline{m_{\mathrm{H}}}$	$\overline{m_{\mathrm{A}}}$	$<m_{\mathrm{H}}>$	$<m_{\mathrm{A}}>$	CL_b	$\boldsymbol{m_{\mathrm{H}}}$	$\boldsymbol{m_{\mathrm{A}}}$
minimal, 1	**Excluded to theoretical limit**									
minimal, 50	**7.9**	**7**	**4.7**	69.1	69.1	70.9	70.9	40%	**71.5**	**71.6**
typical, 1	**10.3**	**13**	**6.1**	86.6	187	87.2	212	55%	**87.0**	**209**
typical, 50	**6.9**	**5**	**4.2**	71.2	72.1	72.2	73.1	36%	**72.7**	**73.6**
maximal, 1	**10.3**	**13**	**6.1**	85.6	183	87.2	208	54%	**87.0**	**204**
maximal, 50	**7.9**	**7**	**4.7**	68.9	68.9	70.4	70.5	43%	**71.4**	**71.5**

Table 9: Higgs mass limits in the MSSM. The number of expected background events, data observed and signal expected events at the at 95% CL. $\overline{m}$ and $< m >$ are respectively the average and median mass limits for the h and A bosons. CL_b is the probability to obtain a mass limit on m_{H} larger than the one observed. The mass limits in boldface are the actual limits set at the 95% CL.

References

[1] F. Zwirner,, "Extensions of the Standard Model", CERN-PH/9601300.

[2] P. Fayet, Phys. Lett. **B 69** (1977) 489.

[3] P. Fayet, Phys. Lett. **B 64** (1976) 159.

[4] P. Fayet and S. Ferrara, Phys. Rev. **C 32** (1977) 249.

[5] H. P. Nilles, Phys. Rev. **110** (1984) 1.

[6] H. E. Haber and G. L. Kane, Phys. Rev. **117** (1985) 75.

[7] M. Carena, M. Quiros and C. E. M. Wagner (CERN), Nucl. Phys. **B 461** (1996).

[8] B. Adeva *et al.*, L3 Collaboration, Nucl. Instr. Meth. **A 289** (1990).

[9] J.A. Bakken *et al.*, Nucl. Instr. Meth. **A 275** (1989).

[10] O. Adriani *et al.*, Nucl. Instr. Meth. **A 302** (1991).

[11] B. Adeva *et al.*, L3 Collaboration Nucl. Instr. Meth. **A 323** (1992).

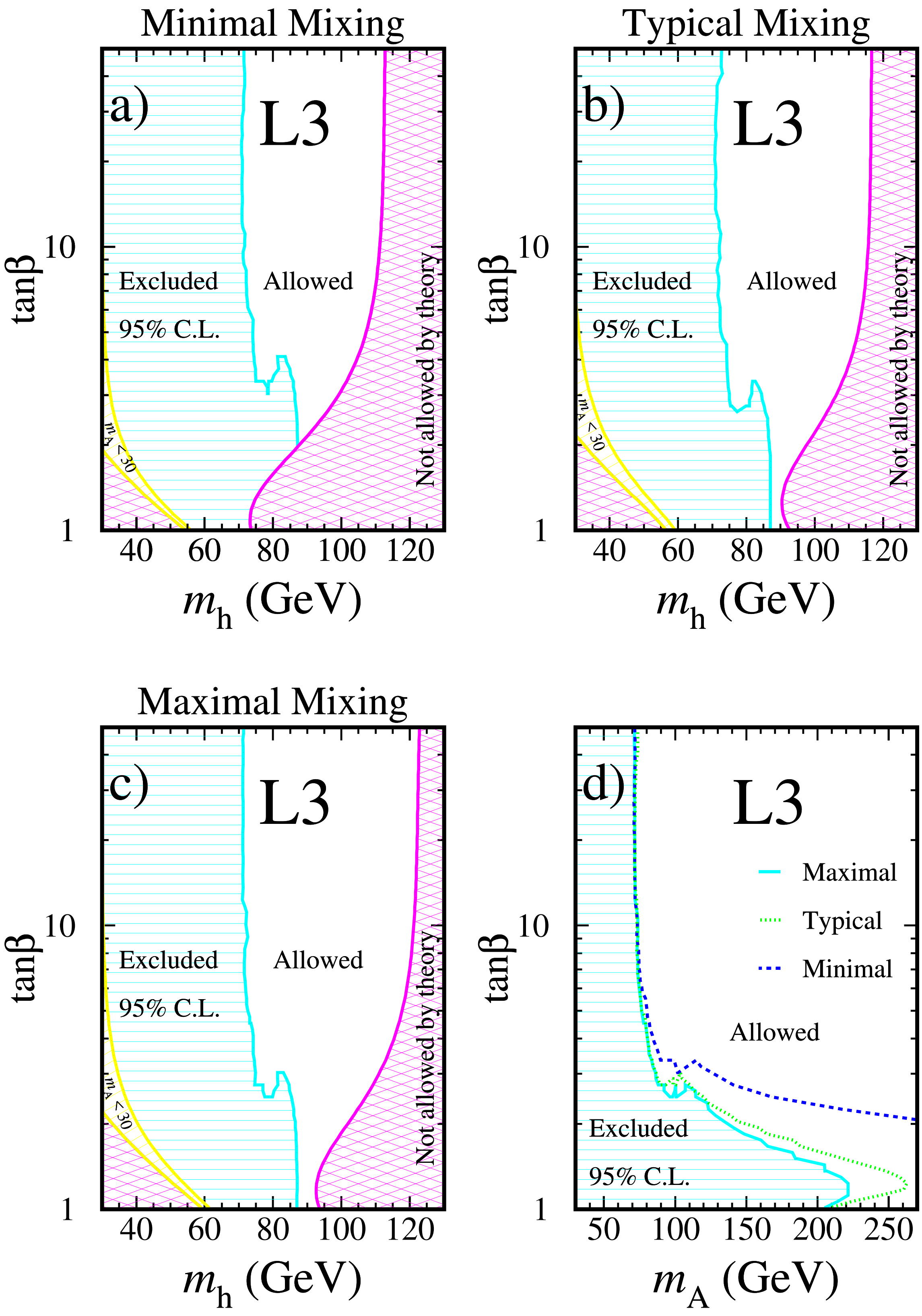

Figure 7: Exclusion plots of the Higgs mass versus $\tan\beta$ at the 95% confidence level from the data collected at $\sqrt{s}$=130-183 GeV. In all the plots, the area shaded by horizontal lines is the 95% CL exclusion; the white area is the non-excluded region; the cross-hatched area is disallowed by theory and the area in the lower left hand corner of plots a, b and c between the 95% exclusion and the theoretically excluded regions represents the lower boundary of the scan over $m_{\rm A}$ which starts at 30 GeV. **a)** 95% CL exclusion of $m_{\rm H}$ versus $\tan\beta$ in the minimal mixing scenario. **b)** Same as (a) but for typical mixing. **c)** Same as (a,b) but for maximal mixing. **d)** 95% CL exclusion of $m_{\rm A}$ versus $\tan\beta$ in the three mixing scenarios. The solid line is the maxing mixing exclusion, the dotted line is typical mixing, and the dashed lined is minimal mixing.

[12] K. Deiters *et al.*, Nucl. Instr. Meth. **A 323** (1992).

[13] M. Chemarin *et al.*, Nucl. Instr. Meth. **A 349** (1994).

[14] B. Acciari *et al.*, Nucl. Instr. Meth. **A 351** (1994).

[15] G. Basti *et al.*, Nucl. Instr. Meth. **A 374** (1996).

[16] A. Adam *et al.*, Nucl. Instr. Meth. **A 383** (1996).

[17] P. Janot, "The HZHA Generator", Physics at LEP2 vol.2, ed. G. Altarelli, T. Sjöstrand, F. Zwirner, CERN 96-01,1996.

[18] T. Sjöstrand, "PYTHIA", CERN-TH/93-7112.

[19] T. Sjöstrand, Comp. Phys. Comm., **82** (1994).

[20] M. Skrzypek *et al.*, Comp. Phys. Comm., **94** (1996).
M. Skrzypek *et al.*, Phys. Lett., **B 232** (1996).

[21] S. Jadach *et al.*, Comp. Phys. Comm., **66** (1991).

[22] R. Engel *et al.*, Z. Phys., **C 66** (1995).
R. Engel *et al.*, Phys. Rew., **D 52** (1995).

[23] F. A. Berends *et al.*, Comp. Phys. Comm., **B 85** (1995).

[24] R. Brun *et al.*, preprint CERN DD/EE/84-1 (Revised 1987).

[25] H. Fesefeldt, RWTH Aachen Report PITHA 85/02 (1985).

[26] M. Acciarri *et al.*, L3 Collaboration, CERN-EP 98-052, to be published on Phys. Lett.

[27] J. Branson *et al.*, "UCSD B Tagging in 1996", L3 Internal Note 2108.

[28] M. Biasini *et al.*, "Standard Model Higgs searches at $\sqrt{s}$ =183 GeV", L3 Internal Note 2241 (See section 3.2 for description of cut optimizer).

[29] M. Acciarri *et al.*, L3 Collaboration, Phys. Lett. **B 385** (1996) 454.

[30] S. Bethke *et al.*, Nucl. Phys. **B 370** (1992) 310.

[31] M. Acciarri *et al.*, L3 Collaboration, Phys. Lett. **B 411** (1997) 373.

[32] M. Acciarri *et al.*, L3 Collaboration, Phys. Lett. **B 413** (1997) 191.

[33] The Working Group on LEP Energy, private communication.

[34] B. A. Kniehl, Phys. Rep. **240 C** (1994) 211;
E. Gross, B. A. Kniehl and G. Wolf, Z. Phys. **C 63** (1994) 417; erratum-ibid **C 66** (1995) 321.

[35] M. Krämer, W. Kilian and P. M. Zerwas, Phys. Lett. **B 373** (1996) 135.

[36] A. Djouadi *et al.*, Z. Phys. **C 70** (1996) 427.

[37] M. Acciarri *et al.*, L3 Collaboration, Phys. Lett. **B 411** (1997) 330.

[38] A. Accomando *et al.*, Physics at LEP2 vol.2 ed. G. Altarelli, T. Sjöstrand, F. Zwirner CERN 96-01,1996.

[39] O. Adriani *et al.*, L3 Collaboration, Phys. Lett. **B 294** (1992) 457.

[40] O. Adriani *et al.*, L3 Collaboration, Z. Phys., **C 57** (1993), 355.

[41] D. Buskulic *et al.*, ALEPH Collaboration, Phys. Lett. **B 313** (1993) 312.

[42] R. Barate *et al.*, ALEPH Collaboration, Phys. Lett. **B 412** (1993) 173.

[43] P. Abreu *et al.*, DELPHI Collaboration, Z. Phys., **C 67** (1995), 69.

[44] P. Abreu *et al.*, DELPHI Collaboration, "Search for Neutral and Charged Higgs Bosons in e^+e^-collisions at $\sqrt{s} = 161$ GeV and 172 GeV", CERN-EP/97-085, Accepted by E. Phys. J. **C**.

[45] R. Akers *et al.*, OPAL Collaboration, Z. Phys., **C 64** (1994), 1.

[46] G. Alexander *et al.*, OPAL Collaboration, Z. Phys., **C 73** (1997), 189.

[47] K. Ackerstaff *et al.*, OPAL Collaboration, "A Search for Neutral Higgs Bosons in the MSSM and Models with Two Scalar Field Doublets", CERN-EP/98-029, Submitted to E. Phys. J. **C**.

[48] A. Favara and M. Pieri, "New Method of Analysis Optimization", L3 Internal Note 2066 (1997).